

Dynamic Gaussians Mesh: Consistent Mesh Reconstruction from Monocular Videos

Isabella Liu¹, Hao Su^{1†}, and Xiaolong Wang^{1†}

University of California, San Diego

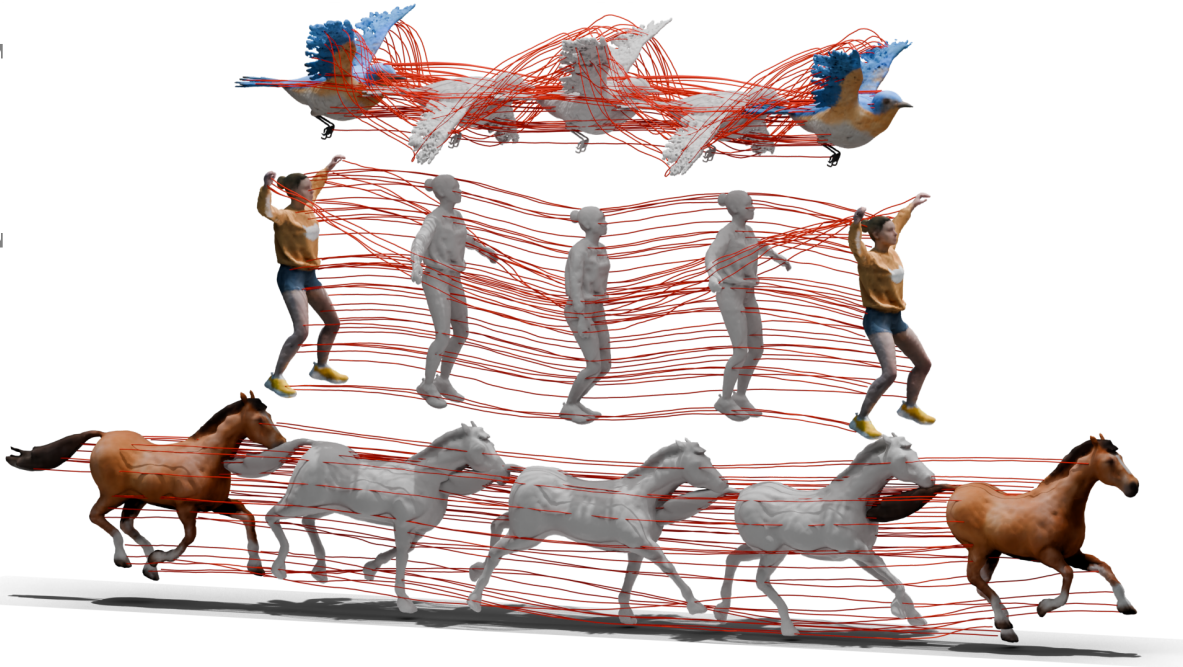


Fig. 1: We propose DG-Mesh, a framework that reconstructs high-fidelity time-consistent mesh from monocular videos. Given monocular inputs of dynamic scenes and the camera parameters, our method reconstructs the high-quality surface and its appearance, as well as the mesh vertice motion across time frames. Our method can reconstruct mesh with flexible topology change. We can reconstruct satisfying surfaces even in challenging thin structures like bird wings.

Abstract. Modern 3D engines and graphics pipelines require mesh as a memory-efficient representation, which allows efficient rendering, geometry processing, texture editing, and many other downstream operations. However, it is still highly difficult to obtain high-quality mesh in terms of structure and detail from monocular visual observations. The problem becomes even more challenging for dynamic scenes and objects. To this end, we introduce Dynamic Gaussians Mesh (DG-Mesh), a framework to reconstruct a high-fidelity and time-consistent mesh given a single monocular video. Our work leverages the recent advancement in 3D Gaussian Splatting to construct the mesh sequence with temporal consistency from a video. Building on top of this representation, DG-Mesh recovers high-quality meshes from the Gaussian points and can track the

mesh vertices over time, which enables applications such as texture editing on dynamic objects. We introduce the Gaussian-Mesh Anchoring, which encourages evenly distributed Gaussians, resulting better mesh reconstruction through mesh-guided densification and pruning on the deformed Gaussians. By applying cycle-consistent deformation between the canonical and the deformed space, we can project the anchored Gaussian back to the canonical space and optimize Gaussians across all time frames. During the evaluation on different datasets, DG-Mesh provides significantly better mesh reconstruction and rendering than baselines.

Keywords: Dynamic Scene Reconstruction · Surface Reconstruction · Neural Rendering

1 Introduction

The birds fly, the butterflies flutter, and the flowers sway with the breeze from the wind – Our natural world is dynamic, and objects present in the human eyes as an entanglement of structure, motion, and color. A pivotal goal in computer vision is to empower machines with the human-like ability to recover object geometry and motion from visual cues in the environment.

The advent of neural rendering techniques has sparked a surge in research focused on extracting the geometry and motion of dynamic scenes from monocular videos using neural representations. Most studies have concentrated on learning deformable neural radiance fields using volumetric representations [21]. However, these volumetric models often fall short in terms of memory efficiency and explicit geometric details. The recent introduction of 3D Gaussian Splatting [13] shifts towards point cloud representations that not only are more memory-efficient but also can provide explicit geometries and superior rendering quality. Further advancements demonstrate how 3D Gaussian Splatting’s explicit geometry can effectively represent dynamic scenes by tracking each point’s movement across frames [20, 39, 49].

This paper takes a significant step in the realm of explicit geometry and motion estimation for dynamic scenes captured as a monocular video. We introduce a method to extract high-fidelity meshes and their motions by tracking vertices over time from a monocular video, as illustrated in Fig. 3. Meshes, in contrast to volume, offer a more memory-efficient format. The mapping of correspondences on mesh vertices greatly simplifies texture editing and propagation on target objects. Crucially, the dynamic mesh extracted via our method can be seamlessly integrated into a physical simulator, enabling rapid, physics-based rendering adaptable to diverse materials and lighting conditions.

Our method, Dynamic Gaussians Mesh (DG-Mesh), performs a joint optimization procedure of both 3D Gaussians and the corresponding meshes. Our method not only allows the mesh to have flexible topology changes but also builds the correspondence across meshes over time. Specifically, our method constructs a set of deformable 3D Gaussians by optimizing the 3D Gaussians in a *canonical space* and learning the deformation module for transforming the 3D Gaussians

in different time steps for rendering. For each time step, we transform the deformed Gaussians into a mesh in a differentiable manner using a combination of Poisson solver and marching cube algorithm, which is then rendered with a differentiable rasterizer for training. Notably, this fully differentiable pipeline allows the change of mesh topology while maintaining cross-frame consistency implicitly due to the introduction of the canonical space. But how do we find the correspondences given these independent meshes?

We achieve this by decomposing the mesh-to-mesh correspondence into two separate correspondences that are easier to acquire: the *mesh-to-points* correspondence that maps the mesh faces to the Gaussian points in each time frame; and the *points-to-canonical-points* correspondence that helps tracking the movement of mesh across time. Our key observation is that the direct training of 3D Gaussians mentioned above will lead to uneven spreading of Gaussians in 3D space (as shown in Fig. 2 left). However, this is detrimental for mesh reconstruction performance due to the violation of the Poisson solver assumption that points should be evenly distributed; worse still, non-uniform Gaussians make it trickier to track across a long time period. Thus, we propose the **Gaussian-Mesh Anchoring** procedure during training, which yields uniformly distributed Gaussians at each frame. Concretely, first, we encourage deformed 3D Gaussians in each time step to align with the corresponding mesh surface that has uniform face distribution due to the underlying iso-surface algorithm; and second, we allow adding Gaussians *in the world frame at each time step* if certain mesh faces are not covered by existing deformed Gaussians, as well as deduplicating Gaussians for mesh faces that are covered multiple times. We call the new set of Gaussians with 1-1 correspondences to mesh faces as *anchored Gaussians*. As depicted in Fig. 2, anchored Gaussians spread more uniformly in 3D.

Finally, we need to update the canonical space to accommodate the added and removed Gaussians in the world frame so that canonical and anchored Gaussians are always consistent. This can be done by introducing a backward deformation network that computes the deformation from the anchored Gaussians to the canonical Gaussians, by which we can inject new Gaussians in the canonical space or remove unnecessary Gaussians. We define a **Cycle-Consistent Deformation** loss inspired by [48], where the cycle is formed with: a forward deformation from the canonical Gaussians to deformed Gaussians, an anchoring process modifying the deformed Gaussians to the anchored Gaussians, a backward deformation from anchored Gaussians to canonical Gaussians. As a result, we obtain uniformly distributed 3D Gaussians in each time step, and they are aligned with the mesh faces. This makes finding the correspondences between meshes much easier.

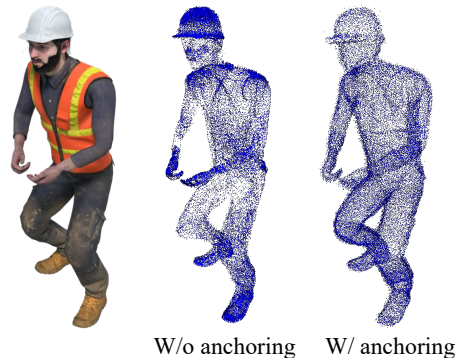


Fig. 2: 3D Gaussian points before and after applying our Gaussian-Mesh Anchoring.

We demonstrate high-fidelity mesh reconstruction and tracking in our experiments. A few examples can be found in Fig. 1, where the correspondence is shown as the red curves connecting the vertices across time. Even for challenging geometries (e.g., thin structures like bird wings), our method can still perform reconstruction and achieve much better results than previous approaches, which usually fail to reconstruct the geometry or construct an oversized mesh. We also demonstrate downstream applications, such as texture editing with our extracted mesh and correspondence (Fig. 8), which is much harder to achieve with non-mesh representations. To the best of our knowledge, this is the first framework that recovers high-fidelity meshes with cross-frame correspondences from monocular videos.

2 Related Work

View Synthesis in a Dynamic Scene. The rise of Neural Radiance Fields (NeRFs) [21] has largely transformed 3D scene reconstruction and novel view synthesis. Its success has also been extended to dynamic scenes in two directions. One direction is to build dynamic NeRFs [4, 7, 16, 41] which models the motion of the scene by extending the radiance field with an extra time dimension or a latent code. To achieve faster rendering speed and more efficient use of memory, recent works perform volume factorization converting the 4D volume into multiple lower dimension planers or tensors [1, 6, 29, 42]. Another direction is to construct an additional deformation field that maps point coordinates in different time frames into a canonical space, where large motion and geometry changes can be captured and learned [5, 23, 24, 27, 35]. The recently proposed 3D Gaussians Splatting [13] extends the volumetric rendering in NeRF by accommodating point clouds. This not only largely improves the speed of neural rendering but also extracts an explicit point cloud structure from images. When applied to dynamic scenes, the same idea of building a deformation field is applied with 3D Gaussians [20, 39, 49]. But instead of an implicit field, the deformation field here explicitly tracks the canonical point clouds over time. Inspired by this line of research, we push forward the reconstruction of explicit geometry representation by using meshes with the tracks of the mesh vertices over time from a monocular video.

Dynamic Mesh Reconstruction. Mesh plays an important role in modern 3D engines, which are widely used for simulation, modeling, and rendering applications. Recovering mesh from static scenes has been extensively studied over the years. Mesh template-based methods [8, 12, 15, 22, 37, 43] optimize the vertex positions from a template to align with the object surface. They usually assume the template is a sphere or a given prior shape, and learn to deform the template into the desired shape to match with the input images. However, when extended to dynamic scenes, these methods often fail because of the topology change during the deformation. Another line of work extract meshed from the implicit field, which can easily handle topology change during deformation. In particular, the mesh can be extracted by identifying and triangulating the zero level sets with methods like Marching Cubes [3], Marching Tetrahedra [34],

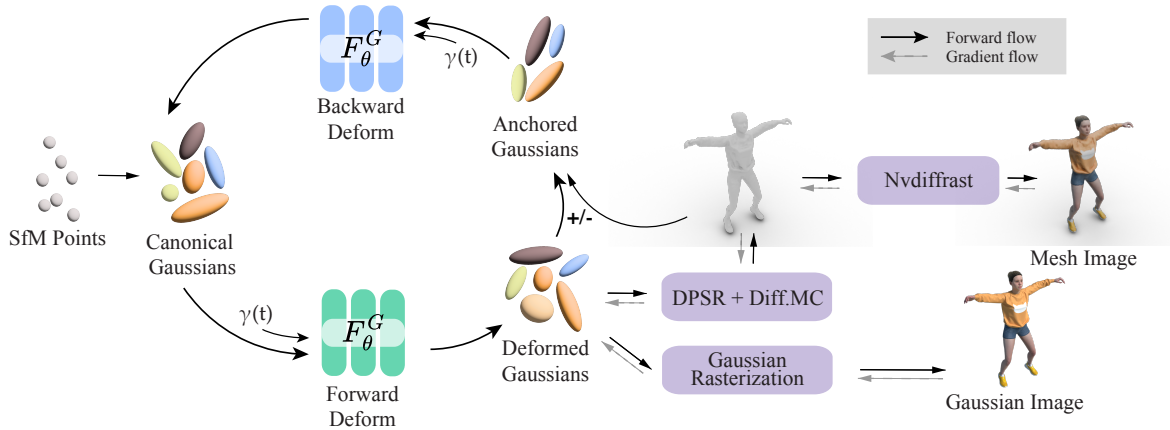


Fig. 3: Main pipeline of DG-Mesh. We maintain a set of canonical 3D Gaussians. Under each time step, we transform it into a deformed space. We treat each set of deformed Gaussian points as an oriented point cloud and apply a differentiable Poisson Solver and differentiable Marching Cubes to recover the deformed surface. We propose Gaussian-Mesh Anchoring to adjust the deformed Gaussians to be uniformly aligned with the mesh faces. During anchoring, Gaussian densification and pruning are performed. We use a backward deformation module to project the newly adjusted Gaussian points back to the canonical space.

and Dual Contouring [10]. Recently, differentiable mesh extraction methods have been proposed [2, 17, 28, 30, 31, 38], directly optimizing mesh through implicit field. Besides static scenes, several works have been studying extracting the surface geometry of deformable objects from dynamic monocular inputs [9, 36, 40, 44–47], which are more closely related to real-world scenarios. Due to the limited information provided by monocular inputs, these methods either rely on category template information or require strong regularization or data modalities to output satisfying results.

3 Method

In this section, we present our framework shown in Fig. 3. Given monocular inputs from a dynamic scene, as well as the time label and camera parameters for each input, we reconstruct the dynamic mesh and its appearance, along with the mesh vertex’s motion trajectory. The surface correspondence across times benefits many downstream applications, such as dynamic texture editing, which propagates the editing under a single frame to the rest of the frames.

Our method maintains a set of canonical 3D Gaussians and deformation networks to deform the Gaussians into different times (Sec. 3.1). We use a differentiable Poisson Solver and a differentiable Marching Cubes method to reconstruct the oriented 3D Gaussian points into meshes (Sec. 3.2). Our model allows the mesh-to-mesh correspondence. This is constructed by two types of correspondence, including the *mesh-to-point* correspondence under each time step and the *point-to-canonical-point* correspondence across all time frames. We propose the **Gaussian-Mesh Anchoring** to encourage the 1-1 correspondence between

the mesh faces and the Gaussians, producing more uniformly distributed *anchored Gaussians*. The **Cycle-Consistent Deformation** maintains the points to canonical points correspondence, which includes a backward deformation network that computes the deformation from the anchored Gaussians to the canonical Gaussians (Sec. 3.3). Finally, we combine all the training objectives (Sec. 3.4).

3.1 Deformable 3D Gaussian Splatting

3D Gaussian Splatting. Recently, 3D Gaussians Splatting (3DGS) [13] has adopted a novel approach based on point cloud rendering, achieving optimal results in novel viewpoint synthesis and scene modeling. In our work, 3DGS provides a fast modeling to explicit geometry and motion, allowing a high-quality and efficient surface reconstruction from the 3D Gaussian point cloud.

We define each 3D Gaussian G by a position (mean) μ , a full 3D covariance matrix Σ centered at point (mean) μ , and the opacity α :

$$G(x; \mu, \Sigma) \propto \exp\left(-\frac{1}{2}(x - \mu)^T \Sigma^{-1}(x - \mu)\right)$$

During the α -blending process, each Gaussian is multiplied by α . To project 3D Gaussians onto image space for rendering, we construct a covariance matrix Σ' through $\Sigma' = JW\Sigma W^T J^T$, where J is the Jacobian of the affine approximation of the projective transformation and W is a viewing transformation (world-to-camera transformation matrix). To ensure a positive semi-definite matrix during the optimization process, Σ is decomposed into a scaling matrix S and a rotation matrix R : $\Sigma = RSS^T R^T$. In our implementation, we directly optimize a 3D vector for scaling s and a quaternion r to represent rotation during the training process. Each 3D Gaussian can now be represented as $G(x; \mu, r, s, \alpha)$.

Deformable 3D Gaussians. 3DGS assumes static scenes and its performance drops drastically when reconstructing dynamic scenes. Several works [11, 18, 39, 49, 50] have investigated the way to extend the 3DGS to dynamic reconstruction and an efficient way is to maintain a canonical 3D Gaussians set. We define a transformation function \mathcal{F} which transforms the 3D Gaussian $G(x; \mu, r, s, \alpha)$ from one space to another by:

$$\mathcal{F}(\gamma(x), \gamma(t)) = (\delta x, \delta r, \delta s, \delta \alpha)$$

, where γ is the positional encoding function to map x and t to higher dimensional Fourier features [32] to enhance detailed reconstruction:

$$\gamma^k(p) \rightarrow (\sin(2^0 \pi p), \cos(2^0 \pi p), \dots, \sin(2^k \pi p), \cos(2^k \pi p))$$

The deformed 3D Gaussian in the new space can be represented by:

$$G'(x + \delta x; \mu, r + \delta r, s + \delta s, \alpha + \delta \alpha)$$

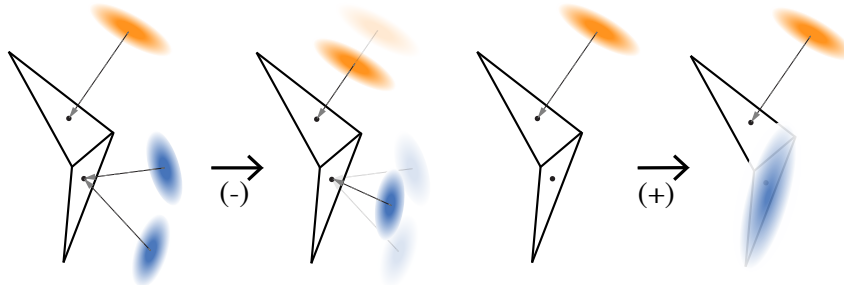


Fig. 4: Illustration of our Gaussian-Mesh Anchoring procedure. After obtaining mesh from the DPSR and differentiable Marching Cubes, we adjust the deformed 3D Gaussians to make it more aligned with the mesh’s faces. For each Gaussian point, we find its nearest neighbors. If a mesh face is the nearest neighbor to multiple Gaussian points at the same time, we merge these Gaussians and create a new Gaussian from them. If a mesh face is not any Gaussian point’s nearest neighbor, we create a new Gaussian on its center.

3.2 Mesh Reconstruction

Surface Extraction and Rendering Pipeline. To apply the isosurface algorithms (such as Marching Cubes [19] or DMTet [30]) and extract the surface geometry from the point-cloud representation of the 3DGS, an indicator function $\chi(x)$ is required over the 3D grid to describe the geometry. Some work [33] query a density grid using 3D Gaussian’s opacity, which does not satisfy the zero derivative condition in the non-boundary space and is computationally inefficient. Instead, we treat 3DGS as an oriented point-cloud and perform a differentiable Poisson solver (DPSR) [26] to obtain the $\chi(x)$. We then apply differentiable Marching Cubes [38] to generate watertight manifold meshes from the obtained value grid. We additionally optimize vertex color for the mesh and perform differentiable rasterization [14] to render the final image.

Laplacian Regularization. To better preserve the mesh surface tessellation, we adopt a mesh Laplacian regularization term to penalize local curvature changes. We use a uniformly weighted differential δ_i of vertex v_i to describe the difference between the position of vertex v_i and the average position of its neighbors. The Laplacian regularization term is the mean square δ_i for all vertices in the mesh, and n is the total number of vertices of the mesh.

$$\mathcal{L}_{lap} = \frac{1}{n} \sum_{i=0}^n \|\delta_i\|^2, \delta_i = v_i - \frac{1}{|N_i|} \sum_{k \in N_i} v_k,$$

where N_i is the one-ring neighbor set of vertex v_i .

3.3 Dynamic Mesh Correspondence

We construct our mesh-to-mesh correspondence with two separate correspondences: the *mesh-to-points* correspondence which maps the mesh faces to the

Gaussian points in each time frame, and the *point-to-canonical-point* correspondence across all time frames that helps tracking the movement of mesh over time.

Gaussian-Mesh Anchoring. To build the *mesh-to-point* correspondence at each time frame, we introduce the Gaussian-Mesh Anchoring. The original 3D Gaussian densification and deformation mechanism leads to uneven spreading of Gaussians in 3D space (Fig. 2), which is undesirable for finding the 1-1 correspondence between mesh and the Gaussians. On the other hand, DPSR discretizes the function values and differential operators in the Poisson equation by assuming the normal vector field n and indicator function χ are uniformly sampled along each dimension. However, this uniformity is not guaranteed during the above training procedure. To encourage the uniformity of the 3D Gaussian distribution, we use reconstructed mesh to guide the densification and pruning of the 3D Gaussian in the deformed space. Specifically, given a deformed 3D Gaussian set $\{G(x_i)\}_{i=0}^N$ and the set of the face centroids from its reconstructed mesh $\{f_j\}_{j=0}^M$ and $N \neq M$. For each 3D Gaussian point x_i we find its nearest neighbor in the mesh face set:

$$n_{x_i} = \arg \min_f \|x_i - f\|, f \in \{f_j\}_{j=0}^M$$

During the densification and pruning process, as shown in Fig. 4, for face f_j that is the nearest neighbor to multiple K Gaussian points, we prune the original K Gaussians and create a new Gaussian by averaging the properties from the K Gaussians:

$$G' = \frac{1}{K} \sum_{k=0}^K G(x_k)$$

On the other hand, for face f_j that is not the nearest neighbor to any Gaussian point, we create a new Gaussian at the face centroid:

$$G' = G(f_j)$$

Besides the above Gaussian density control, we also penalize the distance between Gaussian points and face centroid that has one-to-one correspondence by:

$$\mathcal{L}_{anchor} = \frac{1}{n} \sum_{i=0}^n \|x_i - n_{x_i}\|^2,$$

where n is the total number of faces that have a one-to-one correspondence to the 3D Gaussian points. The obtained anchored Gaussians G' are applied in the Cycle-Consistent deformation loss \mathcal{L}_{cycle} which will be introduced in the next paragraph.

Cycle-Consistent Deformation. Deformable 3D Gaussians provide explicit motion and correspondence across times because of their point-cloud representation. During Gaussian-Mesh Anchoring, we align the reconstructed mesh faces and the 3D Gaussian points in each time frame and perform mesh-guided densification and pruning. To update the canonical space to accommodate the anchored

Gaussians and build the *point-to-canonical-point* correspondence, we encourage the cycle consistency between the canonical and deformed spaces to ensure that the anchoring performed under the deformed space can be applied back to the canonical space. We define a forward transformation function \mathcal{F}_f and a backward transformation function \mathcal{F}_b . Given a canonical 3D Gaussian G and its new form G' under deformed space, we have:

$$\mathcal{F}_f(G, t) = -\mathcal{F}_d(G', t)$$

We use the L_1 loss between \mathcal{F}_f and $-\mathcal{F}_d$ as our cycle consistent loss \mathcal{L}_{cycle} . This cycle-consistent deformation allows the anchored Gaussian to be deformed back to the canonical space. Specifically, G' will be the anchored Gaussians after the Gaussian-Mesh Anchoring, as introduced previously. This cycle-consistency constraint will encourage adjustments to the canonical Gaussians. This process is visualized on the left side of Fig. 3, where the green network is the forward deformation and the blue network is the backward deformation.

3.4 Combining All Training Objectives

We use rendering loss from both mesh rasterization (“Mesh Image” in Fig. 3) and the 3DGS (“Gaussian Image” in Fig. 3) to optimize the mesh geometry and appearance. Given the ground truth image I_{gt} and the Gaussian splatted image I_{gs} . The image loss term of 3DGS can be described as:

$$\mathcal{L}_{gs} = (1 - \lambda_{ssim}) \cdot \|I_{gs} - I_{gt}\| + \lambda_{ssim} \cdot \mathcal{L}_{ssim}(I_{gs}, I_{gt})$$

Same for the rasterized mesh image loss \mathcal{L}_{mesh} . We also compute the L_1 loss on the rasterized mask \mathcal{L}_{mask} .

The Laplacian loss term \mathcal{L}_{lap} in Sec. 3.2 helps preserve the mesh surface tessellation and produces smoother surface. The anchoring loss term \mathcal{L}_{anchor} and the cycle-consistency loss term \mathcal{L}_{cycle} described in Sec. 3.3 help the optimization of cross-frame mesh-to-mesh correspondence. The final loss term can be described as:

$$\begin{aligned} \mathcal{L} = & \mathcal{L}_{gs} + \mathcal{L}_{mesh} + \mathcal{L}_{mask} \\ & + \mathcal{L}_{lap} + \mathcal{L}_{anchor} + \mathcal{L}_{cycle} \end{aligned}$$

4 Experiments

We introduce the dataset we evaluate on and our implementation details in Sec. 4.1 and Sec. 4.2. In Sec. 4.3, we evaluate our method compared with other baselines. Regarding the baselines, we primarily compare with the following works: D-NeRF [27], K-Plane [6], HexPlane [1], TiNeuVox [5]. Among these baselines, D-NeRF [27] and TiNeuVox [5] learn a deformation field to transform the dynamic scene into the canonical space, while other methods like HexPlane [1] and K-Plane [6] utilize volume factorization to learn a compact 4D feature volume. Note that all these baselines do not model scene geometry explicitly, to

Method	Corresp.	Duck				Horse				Bird			
		CD ↓	EMD ↓	PSNR ↑	PSNR _m ↑	CD ↓	EMD ↓	PSNR ↑	PSNR _m ↑	CD ↓	EMD ↓	PSNR ↑	PSNR _m ↑
D-NeRF	✗	0.934	0.073	29.785	23.019	1.685	0.280	25.474	17.381	1.532	0.163	23.848	19.573
K-Plane	✗	1.085	0.055	33.360	20.372	1.480	0.239	28.111	21.629	0.742	0.131	23.722	19.559
HexPlane	✗	2.161	0.090	32.108	27.945	1.750	0.199	26.779	22.395	4.158	0.178	22.189	20.595
TiNeuVox-B	✗	0.969	0.059	34.326	22.073	1.918	0.246	28.161	18.156	8.264	0.215	25.546	19.844
Ours	✓	0.790	0.047	-	32.890	0.299	0.168	-	27.098	0.557	0.128	-	22.977

Method	Corresp.	Beagle				Torus2sphere				Girlwalk			
		CD ↓	EMD ↓	PSNR ↑	PSNR _m ↑	CD ↓	EMD ↓	PSNR ↑	PSNR _m ↑	CD ↓	EMD ↓	PSNR ↑	PSNR _m ↑
D-NeRF	✗	1.001	0.149	34.470	24.446	1.760	0.250	24.227	13.562	0.601	0.190	28.632	21.146
K-Plane	✗	0.810	0.122	38.329	24.613	1.793	0.161	31.215	15.706	0.495	0.173	32.116	23.008
HexPlane	✗	0.870	0.115	38.034	29.970	2.190	0.190	29.714	22.350	0.597	0.155	31.771	24.214
TiNeuVox-B	✗	0.874	0.129	38.972	25.773	2.115	0.203	28.756	14.985	0.568	0.184	32.806	20.207
Ours	✓	0.639	0.117	-	34.518	1.607	0.172	-	26.605	0.726	0.136	-	28.643

Table 1: Mesh reconstruction results of our method compared with other baselines. We measure the reconstructed mesh’s: Chamfer Distant (CD) and Earth Mover Distance (EMD) with the ground truth mesh. We also measure the volume rendering quality PSNR of the baselines as well as the PSNR of their mesh rendering results. We use , , and to indicate the best, the second best and the third results. Our method produces a better quality mesh among all metrics in general.

compare the mesh quality, we extract mesh from either an implicit density field or an occupancy field queried from the 3D Gaussians. In Sec. 4.4, we studied several regularization factors in our method and provided quantitative results of how each factor affects the final performance. We also show several applications such as ray-tracing and texture editing of the time-consistent mesh we export from DG-Mesh.

4.1 Datasets

The D-NeRF [27] synthetic dataset does not provide mesh ground truth information. Therefore, we rendered a synthetic dataset containing six dynamic scenes to compare the mesh reconstruction quality quantitatively. Each scene includes 200 frames of a moving object with the ground truth camera parameters and images, as well as the ground truth mesh under each time frame. Camera views are evenly distributed around the target objects on the sphere or the upper sphere. We also evaluate our method on D-NeRF synthetic dataset and provide the visualization and comparison with other baselines in Fig. 5. For real data, we run our method on the Nerfies dataset [23] which contains monocular videos of daily life objects captured using hand-held cameras. We provide the visualization of the reconstructed mesh as well as the mesh rendering images in Fig. 7. We also tested our results on the Unbiased4D dataset [9], which provides one sequence of real monocular video captures of a moving cactus toy.

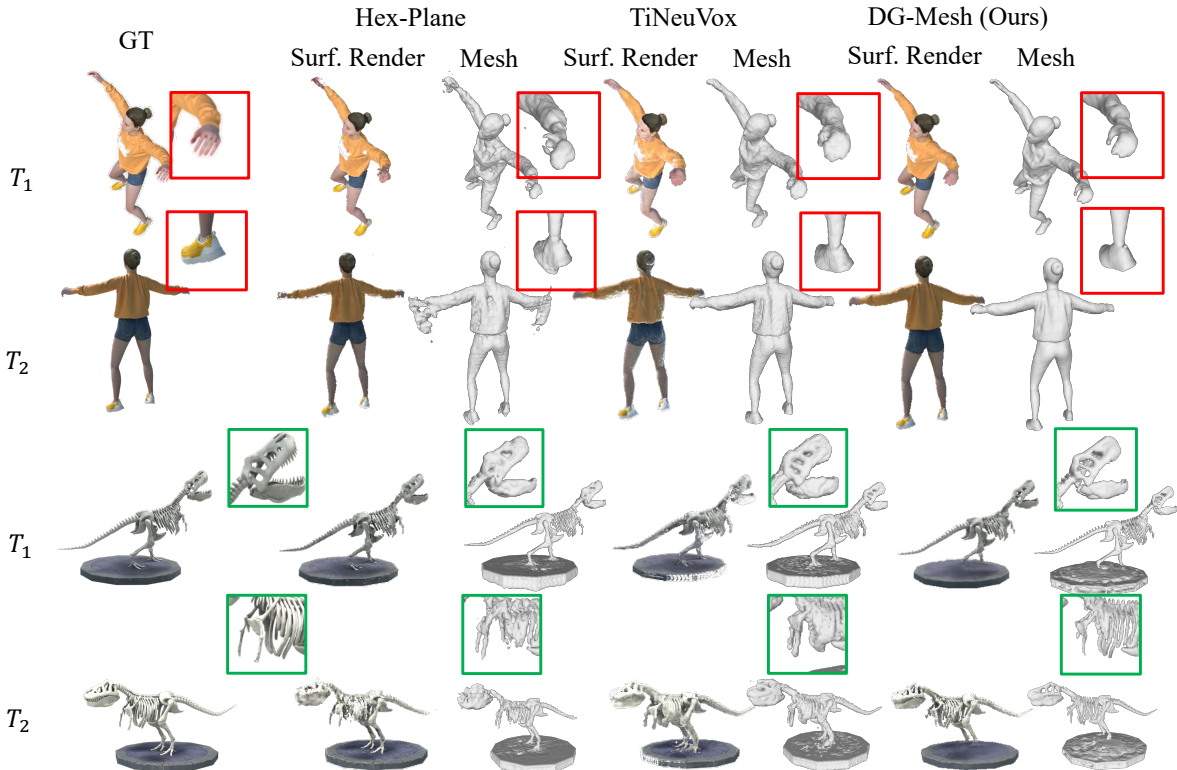


Fig. 5: We compare the mesh reconstruction and rendering results of our method and other baselines on the D-NeRF dataset. For each object, we visualize the results under two different time steps and different viewing angles. Our method outperforms others by producing more smooth and detailed structures.

4.2 Implementation Details

We used PyTorch [25] to implement our method and utilized the implementation from 3D Gaussian Splatting [13] for differential Gaussian rasterization. Our model was trained for a total of 50,000 iterations on a single RTX 3090Ti. To better initialize deformable 3D Gaussians, we first trained the canonical Gaussians for $3k$ iterations while keeping the forward and backward deformation network fixed. This helped to retain relatively stable positions and shapes of 3D Gaussians under the canonical space. After $5k$ iterations, we introduce the DPSR and differentiable Marching Cubes to extract the mesh geometry from the Gaussian points. We perform Gaussian-Mesh Anchoring every 100 iteration during training. For the mesh rasterization, we use Nvdiffrast, to query the vertex color of the deformed mesh, we project the location of the deformed vertex back to the canonical space and query a time-dependent appearance module to obtain the color. We found optimizing the vertex color in canonical space produces better results compared with querying color under different deformed spaces. The final supervision comes from the rendering loss from both the splatted Gaussian images and the rendered mesh images.

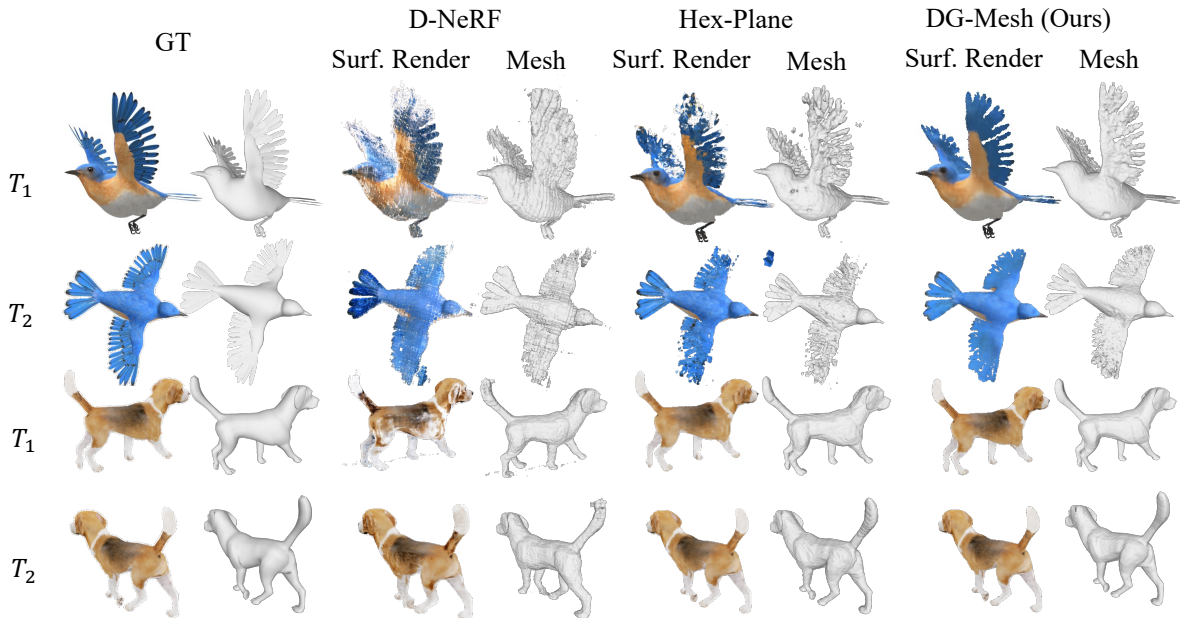


Fig. 6: We provide the result comparison of our method with other baselines in our rendered dataset. Our method gives better mesh rendering quality as well as geometry. For objects such as the flying bird, other methods fail to recover the thin geometry of the bird wings. Instead, our method produces satisfying geometry. Our method also produces better surface rendering.

4.3 Results and Comparisons

For the D-NeRF dataset, we present our numerical results and comparisons in Tab. 2 and mesh visualization in Fig. 5. We compare the mesh rendering PSNR, SSIM, and LPIPS scores for each object in the dataset. Since the D-NeRF dataset does not provide ground truth mesh, we do not numerically evaluate our performance of the mesh quality. In Fig. 5, we highlight the part where our method outperforms the other baselines and recovers the highly detailed structures. For our rendered dataset with mesh ground truth, we provide the numerical results and comparisons in Tab. 1 and visualizations in Fig. 6. Regarding evaluation metrics of mesh quality, we chose two different metrics to measure the accuracy of our mesh reconstruction: the Chamfer Distance (CD) and the Earth Mover Distance (EMD) to measure the displacement between the reconstructed mesh and the ground truth. As shown in Tab. 1, our method achieves lower CD and EMD scores compared with other baselines in general, indicating our method reconstructs the highest quality mesh. In Fig. 6, we show the visualization of our reconstructed mesh compared to other baselines in our dataset. In challenging areas, such as thin structures like the wings of the bird, our method still recovers high-quality geometry and surfaces, while other methods produce floaters or oversized meshes.

4.4 Ablation Study

Laplacian Smoothness Regularizer. We study the effect of laplacian regularizer and its different performance under different loss weights in this part.

Method	Lego			Bouncingballs			Jumpingjacks			Hook		
	PSNR _m ↑	SSIM ↑	LPIPS ↓	PSNR _m ↑	SSIM ↑	LPIPS ↓	PSNR _m ↑	SSIM ↑	LPIPS ↓	PSNR _m ↑	SSIM ↑	LPIPS ↓
D-NeRF	20.384	0.818	0.137	23.398	0.899	0.157	22.255	0.914	0.103	20.300	0.889	0.108
K-Plane	19.523	0.828	0.127	23.307	0.935	0.109	25.240	0.937	0.068	22.503	0.900	0.094
HexPlane	22.872	0.904	0.072	25.389	0.957	0.069	27.078	0.954	0.052	24.513	0.929	0.070
TiNeuVox-B	21.927	0.843	0.126	24.819	0.947	0.101	23.621	0.932	0.075	21.429	0.908	0.085
Ours	21.289	0.838	0.159	29.145	0.969	0.099	31.769	0.977	0.045	27.884	0.954	0.074

Method	Mutant			Standup			Trex			Hellwarrior		
	PSNR _m ↑	SSIM ↑	LPIPS ↓	PSNR _m ↑	SSIM ↑	LPIPS ↓	PSNR _m ↑	SSIM ↑	LPIPS ↓	PSNR _m ↑	SSIM ↑	LPIPS ↓
D-NeRF	21.070	0.906	0.077	23.380	0.925	0.069	22.594	0.908	0.085	18.907	0.877	0.129
K-Plane	23.226	0.923	0.064	25.778	0.946	0.048	23.093	0.921	0.075	18.073	0.881	0.123
HexPlane	26.811	0.953	0.045	27.931	0.965	0.035	26.629	0.953	0.046	21.250	0.917	0.094
TiNeuVox-B	22.967	0.925	0.064	24.263	0.941	0.051	24.219	0.927	0.070	18.657	0.883	0.118
Ours	30.400	0.968	0.055	30.208	0.974	0.051	28.951	0.959	0.065	25.460	0.959	0.084

Table 2: We measure the mesh rendering PSNR, SSIM and LPIPS score of all the baselines and our method on the D-NeRF dataset. Our method has the highest surface rendering quality compared with all the other baselines.

	CD ↓	EMD ↓	PSNR _m ↑	SSIM _m ↑	LPIPS _m ↓
$w_{lap} = 0$	0.972	0.089	31.947	0.971	0.079
$w_{lap} = 100$	1.239	0.093	32.178	0.969	0.069
$w_{lap} = 1000$	0.762	0.073	33.890	0.982	0.061
$w_{lap} = 2000$	0.894	0.069	32.891	0.981	0.072

Table 3: Results of mesh reconstruction and rendering quality with different Laplacian regularizer ratios. When $w_{lap} = 1000$ our method produces the best results. During the training process, we set the Laplacian ratio to be 1000.

Laplacian regularization term calculates the average square Euclidean difference between the vertex and its one-ring neighbors, which discourages deformation that will introduce large surface curvature change. We measure the final mesh rendering quality (PSNR, SSIM, LPIPS) under different laplacian loss weights. As shown in Tab. 3, when $w_{lap} = 1000$, the network produces the highest mesh rendering quality. With appropriate laplacian regularization, our method recovers a smoother surface.

Gaussian-Mesh Anchoring. We study the effect of our proposed Gaussian-Mesh Anchoring procedure. Since the original densification and pruning mechanism of 3DGS tends to split more Gaussian in hard areas where the geometry and appearance are more complicated. The original Gaussian center distribution is not even on the object’s surface. As discussed in Sec. 3.3, DPSR assumes uniformly sampled points among the space. An uneven point cloud on the surface will produce the wrong distance field and harm the optimization process. Our Gaussian-Mesh Anchoring performs densification and pruning that will result in a more evenly distributed Gaussian point and rely on the backward deformation network to project it back to the canonical space. As shown in Fig. 2, after applying Gaussian-Mesh Anchoring, the Gaussian centers are more evenly



Fig. 7: We provide the reconstructed mesh visualization and mesh rendering image of our method on real-world datasets including the Nerfies dataset with monocular videos of daily life objects captured using hand-held cameras; the Unbiased4D dataset contains one sequence of real monocular video captures of a moving toy.

	CD ↓	EMD ↓	PSNR _m ↑	SSIM ↑	LPIPS ↓
w./o. anchor	0.685	0.146	31.283	0.921	0.048
w./ anchor	0.516	0.128	32.734	0.9180	0.041

Table 4: We turn the Gaussian-Mesh Anchoring on and off and measure the reconstructed mesh quality. The results indicate that the anchoring procedures improve the performance by guiding the Gaussian points to deform more evenly on the surface.

distributed on the object’s surface. We provide quantitative results of how the Gaussian-Mesh Anchoring procedure allows the network to produce better geometry in Tab. 4. Without Gaussian-Mesh Anchoring, the reconstructed CD and EMD are both higher, and the mesh rendering is also not as good as it is with the anchoring.

Applications DG-Mesh provides dense correspondence, which is particularly useful for a variety of downstream applications such as shape manipulation and texture editing. We showcase two examples of mesh editing applications enabled by our method in Fig. 8. We can insert the extracted mesh into new scene and perform ray-tracing. Given our time-consistent mesh under the first frame, we edit the mesh vertex’s color in the first frame by painting color to its surface; the same vertex color and pattern are propagated to the following frames. This editing process is straightforward to use.

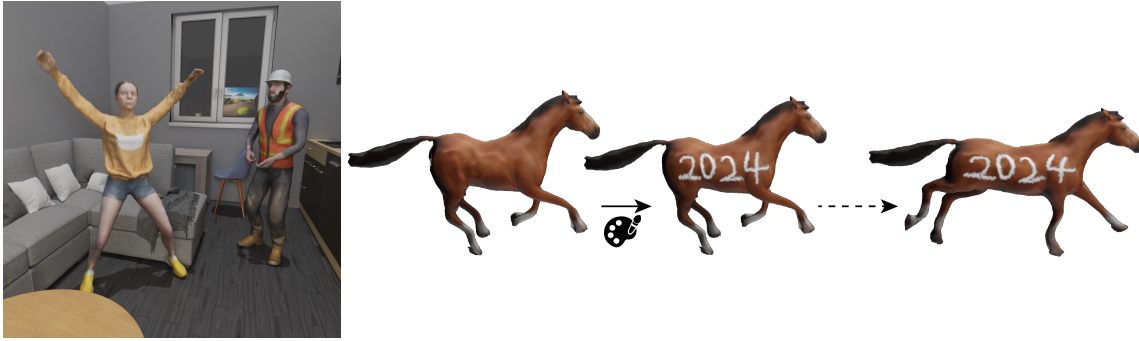


Fig. 8: Two types of application can be done with time-consistent mesh: 1. Ray-tracing in the rendering engine. 2. Texture editing: With correspondence across time frames, we just need to edit the first frame in a sequence and the change will be automatically applied to the rest of the sequence.

5 Conclusion

We introduce Dynamic Gaussians Mesh (DG-Mesh), a framework to reconstruct high-fidelity mesh and perform motion tracking from monocular videos in dynamic scenes. Leveraging the recent advancements in 3D Gaussian Splatting, DG-Mesh learns a deformable 3D Gaussians set and builds a novel time-consistent mesh on top of it. DG-Mesh outperforms previous methods in reconstructing intricate structures like bird wings and horse legs, which are typically difficult to capture. Moreover, DG-Mesh’s ability to provide cross-frame correspondences enables various downstream applications, such as texture editing on dynamic objects, making it a versatile tool with great potential in graphics applications. We will release our code upon paper publication.

Limitations. DG-Mesh is currently applied mainly on the foreground objects in a video. To make DG-Mesh work with real-world videos, we require accurate object segmentation and tracking of the foreground object across the video. While DG-Mesh handles both the correspondence and topology changes, fundamentally, it is very challenging to obtain correspondence when there is a large topology change. For example, if there is an additional object or object part that appears in the video over time, it is hard to find the correspondence for the new object (or object part) when compared to the first frame. This is the limitation of the nature of the problem instead of the limitation of our method.

References

1. Cao, A., Johnson, J.: Hexplane: A fast representation for dynamic scenes. In: Proceedings of the IEEE/CVF Conference on Computer Vision and Pattern Recognition. pp. 130–141 (2023) [4](#), [9](#)
2. Chen, Z., Tagliasacchi, A., Funkhouser, T., Zhang, H.: Neural dual contouring. *ACM Transactions on Graphics (TOG)* **41**(4), 1–13 (2022) [5](#)
3. Cubes, M.: A high resolution 3d surface construction algorithm/william e. Lorensen, Harvey E. Cline–SIG **87**, 76 (1987) [4](#)

4. Du, Y., Zhang, Y., Yu, H.X., Tenenbaum, J.B., Wu, J.: Neural radiance flow for 4d view synthesis and video processing. In: 2021 IEEE/CVF International Conference on Computer Vision (ICCV). pp. 14304–14314. IEEE Computer Society (2021) [4](#)
5. Fang, J., Yi, T., Wang, X., Xie, L., Zhang, X., Liu, W., Nießner, M., Tian, Q.: Fast dynamic radiance fields with time-aware neural voxels. In: SIGGRAPH Asia 2022 Conference Papers. pp. 1–9 (2022) [4](#), [9](#)
6. Fridovich-Keil, S., Meanti, G., Warburg, F.R., Recht, B., Kanazawa, A.: K-planes: Explicit radiance fields in space, time, and appearance. In: Proceedings of the IEEE/CVF Conference on Computer Vision and Pattern Recognition. pp. 12479–12488 (2023) [4](#), [9](#)
7. Gao, C., Saraf, A., Kopf, J., Huang, J.B.: Dynamic view synthesis from dynamic monocular video. In: Proceedings of the IEEE/CVF International Conference on Computer Vision. pp. 5712–5721 (2021) [4](#)
8. Hanocka, R., Metzger, G., Giryas, R., Cohen-Or, D.: Point2mesh: A self-prior for deformable meshes. arXiv preprint arXiv:2005.11084 (2020) [4](#)
9. Johnson, E., Habermann, M., Shimada, S., Golyanik, V., Theobalt, C.: Unbiased 4d: Monocular 4d reconstruction with a neural deformation model. In: Proceedings of the IEEE/CVF Conference on Computer Vision and Pattern Recognition. pp. 6597–6606 (2023) [5](#), [10](#)
10. Ju, T., Losasso, F., Schaefer, S., Warren, J.: Dual contouring of hermite data. In: Proceedings of the 29th annual conference on Computer graphics and interactive techniques. pp. 339–346 (2002) [5](#)
11. Jung, H., Brasch, N., Song, J., Perez-Pellitero, E., Zhou, Y., Li, Z., Navab, N., Busam, B.: Deformable 3d gaussian splatting for animatable human avatars. arXiv preprint arXiv:2312.15059 (2023) [6](#)
12. Kanazawa, A., Tulsiani, S., Efros, A.A., Malik, J.: Learning category-specific mesh reconstruction from image collections. In: Proceedings of the European Conference on Computer Vision (ECCV). pp. 371–386 (2018) [4](#)
13. Kerbl, B., Kopanas, G., Leimkühler, T., Drettakis, G.: 3d gaussian splatting for real-time radiance field rendering. *ACM Transactions on Graphics (ToG)* **42**(4), 1–14 (2023) [2](#), [4](#), [6](#), [11](#)
14. Laine, S., Hellsten, J., Karras, T., Seol, Y., Lehtinen, J., Aila, T.: Modular primitives for high-performance differentiable rendering. *ACM Transactions on Graphics (TOG)* **39**(6), 1–14 (2020) [7](#)
15. Li, X., Liu, S., De Mello, S., Kim, K., Wang, X., Yang, M.H., Kautz, J.: Online adaptation for consistent mesh reconstruction in the wild. *Advances in Neural Information Processing Systems* **33**, 15009–15019 (2020) [4](#)
16. Li, Z., Niklaus, S., Snavely, N., Wang, O.: Neural scene flow fields for space-time view synthesis of dynamic scenes. In: Proceedings of the IEEE/CVF Conference on Computer Vision and Pattern Recognition. pp. 6498–6508 (2021) [4](#)
17. Liao, Y., Donne, S., Geiger, A.: Deep marching cubes: Learning explicit surface representations. In: Proceedings of the IEEE Conference on Computer Vision and Pattern Recognition. pp. 2916–2925 (2018) [5](#)
18. Lin, Y., Dai, Z., Zhu, S., Yao, Y.: Gaussian-flow: 4d reconstruction with dynamic 3d gaussian particle. arXiv preprint arXiv:2312.03431 (2023) [6](#)
19. Lorensen, W.E., Cline, H.E.: Marching cubes: A high resolution 3d surface construction algorithm. In: *Seminal graphics: pioneering efforts that shaped the field*, pp. 347–353 (1998) [7](#)
20. Luiten, J., Kopanas, G., Leibe, B., Ramanan, D.: Dynamic 3d gaussians: Tracking by persistent dynamic view synthesis. arXiv preprint arXiv:2308.09713 (2023) [2](#), [4](#)

21. Mildenhall, B., Srinivasan, P.P., Tancik, M., Barron, J.T., Ramamoorthi, R., Ng, R.: Nerf: Representing scenes as neural radiance fields for view synthesis. *Communications of the ACM* **65**(1), 99–106 (2021) [2](#), [4](#)
22. Pan, J., Han, X., Chen, W., Tang, J., Jia, K.: Deep mesh reconstruction from single rgb images via topology modification networks. in 2019 ieee. In: *CVF International Conference on Computer Vision (ICCV)*. vol. 3 (2019) [4](#)
23. Park, K., Sinha, U., Barron, J.T., Bouaziz, S., Goldman, D.B., Seitz, S.M., Martin-Brualla, R.: Nerfies: Deformable neural radiance fields. In: *Proceedings of the IEEE/CVF International Conference on Computer Vision*. pp. 5865–5874 (2021) [4](#), [10](#)
24. Park, K., Sinha, U., Hedman, P., Barron, J.T., Bouaziz, S., Goldman, D.B., Martin-Brualla, R., Seitz, S.M.: Hypernerf: A higher-dimensional representation for topologically varying neural radiance fields. *arXiv preprint arXiv:2106.13228* (2021) [4](#)
25. Paszke, A., Gross, S., Massa, F., Lerer, A., Bradbury, J., Chanan, G., Killeen, T., Lin, Z., Gimelshein, N., Antiga, L., et al.: Pytorch: An imperative style, high-performance deep learning library. *Advances in neural information processing systems* **32** (2019) [11](#)
26. Peng, S., Jiang, C., Liao, Y., Niemeyer, M., Pollefeys, M., Geiger, A.: Shape as points: A differentiable poisson solver. *Advances in Neural Information Processing Systems* **34**, 13032–13044 (2021) [7](#)
27. Pumarola, A., Corona, E., Pons-Moll, G., Moreno-Noguer, F.: D-nerf: Neural radiance fields for dynamic scenes. In: *Proceedings of the IEEE/CVF Conference on Computer Vision and Pattern Recognition*. pp. 10318–10327 (2021) [4](#), [9](#), [10](#)
28. Remelli, E., Lukoianov, A., Richter, S., Guillard, B., Bagautdinov, T., Baque, P., Fua, P.: Meshsdf: Differentiable iso-surface extraction. *Advances in Neural Information Processing Systems* **33**, 22468–22478 (2020) [5](#)
29. Shao, R., Zheng, Z., Tu, H., Liu, B., Zhang, H., Liu, Y.: Tensor4d: Efficient neural 4d decomposition for high-fidelity dynamic reconstruction and rendering. In: *Proceedings of the IEEE/CVF Conference on Computer Vision and Pattern Recognition*. pp. 16632–16642 (2023) [4](#)
30. Shen, T., Gao, J., Yin, K., Liu, M.Y., Fidler, S.: Deep marching tetrahedra: a hybrid representation for high-resolution 3d shape synthesis. *Advances in Neural Information Processing Systems* **34**, 6087–6101 (2021) [5](#), [7](#)
31. Shen, T., Munkberg, J., Hasselgren, J., Yin, K., Wang, Z., Chen, W., Gojcic, Z., Fidler, S., Sharp, N., Gao, J.: Flexible isosurface extraction for gradient-based mesh optimization. *ACM Transactions on Graphics (TOG)* **42**(4), 1–16 (2023) [5](#)
32. Tancik, M., Srinivasan, P., Mildenhall, B., Fridovich-Keil, S., Raghavan, N., Singhal, U., Ramamoorthi, R., Barron, J., Ng, R.: Fourier features let networks learn high frequency functions in low dimensional domains. *Advances in Neural Information Processing Systems* **33**, 7537–7547 (2020) [6](#)
33. Tang, J., Ren, J., Zhou, H., Liu, Z., Zeng, G.: Dreamgaussian: Generative gaussian splatting for efficient 3d content creation. *arXiv preprint arXiv:2309.16653* (2023) [7](#)
34. Treece, G.M., Prager, R.W., Gee, A.H.: Regularised marching tetrahedra: improved iso-surface extraction. *Computers & Graphics* **23**(4), 583–598 (1999) [4](#)
35. Tretschk, E., Tewari, A., Golyanik, V., Zollhöfer, M., Lassner, C., Theobalt, C.: Non-rigid neural radiance fields: Reconstruction and novel view synthesis of a dynamic scene from monocular video. In: *Proceedings of the IEEE/CVF International Conference on Computer Vision*. pp. 12959–12970 (2021) [4](#)

36. Tulsiani, S., Kulkarni, N., Gupta, A.: Implicit mesh reconstruction from unannotated image collections. arXiv preprint arXiv:2007.08504 (2020) [5](#)
37. Wang, N., Zhang, Y., Li, Z., Fu, Y., Liu, W., Jiang, Y.G.: Pixel2mesh: Generating 3d mesh models from single rgb images. In: Proceedings of the European conference on computer vision (ECCV). pp. 52–67 (2018) [4](#)
38. Wei, X., Xiang, F., Bi, S., Chen, A., Sunkavalli, K., Xu, Z., Su, H.: Neumanifold: Neural watertight manifold reconstruction with efficient and high-quality rendering support. arXiv preprint arXiv:2305.17134 (2023) [5](#), [7](#)
39. Wu, G., Yi, T., Fang, J., Xie, L., Zhang, X., Wei, W., Liu, W., Tian, Q., Wang, X.: 4d gaussian splatting for real-time dynamic scene rendering. arXiv preprint arXiv:2310.08528 (2023) [2](#), [4](#), [6](#)
40. Wu, S., Jakob, T., Ruppel, C., Vedaldi, A.: Dove: Learning deformable 3d objects by watching videos. International Journal of Computer Vision pp. 1–12 (2023) [5](#)
41. Xian, W., Huang, J.B., Kopf, J., Kim, C.: Space-time neural irradiance fields for free-viewpoint video. In: Proceedings of the IEEE/CVF Conference on Computer Vision and Pattern Recognition. pp. 9421–9431 (2021) [4](#)
42. Xu, Z., Peng, S., Lin, H., He, G., Sun, J., Shen, Y., Bao, H., Zhou, X.: 4k4d: Real-time 4d view synthesis at 4k resolution (2023) [4](#)
43. Xue, Y., Bhatnagar, B.L., Marin, R., Sarafianos, N., Xu, Y., Pons-Moll, G., Tung, T.: Nsf: Neural surface fields for human modeling from monocular depth. In: Proceedings of the IEEE/CVF International Conference on Computer Vision. pp. 15049–15060 (2023) [4](#)
44. Yang, G., Sun, D., Jampani, V., Vlasic, D., Cole, F., Chang, H., Ramanan, D., Freeman, W.T., Liu, C.: Lasr: Learning articulated shape reconstruction from a monocular video. In: Proceedings of the IEEE/CVF Conference on Computer Vision and Pattern Recognition. pp. 15980–15989 (2021) [5](#)
45. Yang, G., Sun, D., Jampani, V., Vlasic, D., Cole, F., Liu, C., Ramanan, D.: Viser: Video-specific surface embeddings for articulated 3d shape reconstruction. Advances in Neural Information Processing Systems **34**, 19326–19338 (2021) [5](#)
46. Yang, G., Vo, M., Neverova, N., Ramanan, D., Vedaldi, A., Joo, H.: Banmo: Building animatable 3d neural models from many casual videos. In: Proceedings of the IEEE/CVF Conference on Computer Vision and Pattern Recognition. pp. 2863–2873 (2022) [5](#)
47. Yang, G., Yang, S., Zhang, J.Z., Manchester, Z., Ramanan, D.: Ppr: Physically plausible reconstruction from monocular videos. In: Proceedings of the IEEE/CVF International Conference on Computer Vision. pp. 3914–3924 (2023) [5](#)
48. Yang, K., Zhang, X., Huang, Z., Chen, X., Xu, Z., Su, H.: Movingparts: Motion-based 3d part discovery in dynamic radiance field. arXiv preprint arXiv:2303.05703 (2023) [3](#)
49. Yang, Z., Gao, X., Zhou, W., Jiao, S., Zhang, Y., Jin, X.: Deformable 3d gaussians for high-fidelity monocular dynamic scene reconstruction. arXiv preprint arXiv:2309.13101 (2023) [2](#), [4](#), [6](#)
50. Zielonka, W., Bagautdinov, T., Saito, S., Zollhöfer, M., Thies, J., Romero, J.: Drivable 3d gaussian avatars (2023) [6](#)

“Dynamic Gaussians Mesh: Consistent Mesh Reconstruction from Monocular Videos” Supplementary Material

Isabella Liu¹, Hao Su^{1†}, and Xiaolong Wang^{1†}

University of California, San Diego

A Overview

In this supplementary material, we first introduce more implementation details in Appendix B, including the network architecture, the detailed description of our Gaussian-Mesh Anchoring algorithm, and the training details. In Appendix C, we introduce more information on our rendered dataset. In Appendix D, we show more mesh construction results of our method compared with other baselines on the D-NeRF dataset as well as the DG-Mesh dataset.

B Implementation Details

B.1 Network Architecture and Training Details

For the forward and backward deformation networks, we use an MLP the depth $D = 8$ and the dimension of the hidden layer $W = 256$. An illustration of the network architecture is shown in Fig. 1. We apply positional encoding $\gamma^k(p)$ to map position x and time label t to higher dimensional feature space, and we set $k = 10$ for 3D Gaussian’s positions x and $k = 6$ for time label t . After the last layer, we use a single Linear layer without activation to obtain the predicted Gaussian position offset δx , scaling offset δs , rotation offset δr and the opacity offset $\delta \alpha$. The appearance network uses the similar architecture as the deformation network, while the last layer outputs the RGB color of the input vertex.

During training, we train the first $3k$ iterations without optimizing the parameters in the deformation network, this helps to retain relatively stable positions and shapes of 3D Gaussians under the canonical space. From iteration $8k$, we start to optimize the mesh and its appearance using Differentiable Poisson Solver (DPSR) and Differentiable Marching Cubes (Diff. MC). Starts from iteration $15k$, we perform the Gaussian-Mesh Anchoring every 100 iterations guide the Gaussian points more uniformly distribute on the surface. We train the network for $50k$ iterations in total.

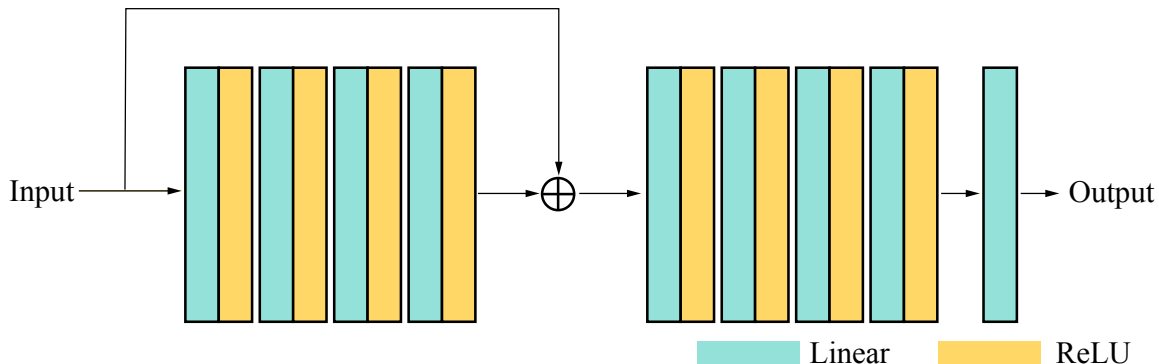


Fig. 1: Illustration of the network architecture

B.2 Gaussian-Mesh Anchoring Algorithm

We use the Gaussian-Mesh Anchoring procedure to guide the Gaussian to be more uniformly distributed on the object’s surface, which results in a smoother mesh reconstruction from DPSR and DiffMC. In Line 1 is a more detailed description of our algorithm. The algorithm first find the nearest mesh face for each Gaussian point. For each mesh face, if it is linked to multiple Gaussian points, merge these Gaussians and create a new one. If a mesh face is only linked to one specific Gaussian, we move this Gaussian towards the face centroid. If a mesh face is not linked to any Gaussian point, we create a new Gaussian using the face centroid.

C Dataset Details

To quantitatively evaluate the mesh reconstruction quality of our method, ground truth mesh is needed. Since the existing dataset (e.g. the D-NeRF dataset) does not provide mesh ground truth information, we use Blender to render our own dataset. Specifically, we render 6 dynamic scenes including a running horse, a flying bird, a walking beagle, a walking duck, a walking cartoon girl, and a deforming sphere. The deforming sphere example is designed to test the method’s ability to handle topology change during deformation (the sphere is gradually deformed into a torus). Our dataset follows the data format from the D-NeRF dataset, which provides camera parameters, RGB images, as well as the ground truth mesh stored in OBJ format.

For rendering specification, we use the Eevee render engine for the running horse scene and the Cycles render engine for the other five scenes. The sampling number is set to 128. The video length for each scene is 200 frames. For both training and testing sets, each frame is only visible under one camera view. The rendered image resolution is 800×800 in s-RGB color space.

Algorithm 1: Gaussian-Mesh Anchoring

```

Data: gaussians, time, verts, faces, deform, deform_back,
        search_radius=0.005
Result: anchor_loss
deformed_gaussian = deform(gaussians, time);
anchor_loss = 0;
for face in faces do
    gs_to_mesh_idx = knn(deformed_gaussian, face.centroid, k=1,
        radius=search_radius);
    selected_gaussians = gaussians[gs_to_mesh_idx == face];
    if count(selected_gaussians) > 1 then
        new_gaussian = merge_gaussians(selected_gaussians);
        canonical_new_gaussian = deform_back(new_gaussian, time);
        gaussians.delete(selected_gaussians);
        gaussians.append(canonical_new_gaussian);
        anchor_loss += distance(canonical_new_gaussian, face);
    end
    else if count(gs_to_mesh_idx == face) == 1 then
        | anchor_loss += distance(selected_gaussians, face);
    end
    else
        | new_gaussian = face.centroid;
        | canonical_new_gaussian = deform_back(new_gaussian, time);
        | gaussians.append(canonical_new_gaussian);
    end
end

```

D Results on the D-NeRF and DG-Mesh Dataset

We provide more results visualization of our method as well as the other baselines on the D-NeRF dataset and the DG-Mesh dataset. From Fig. 2 - Fig. 4 are the results on the DG-Mesh dataset. For each data sample, We show the reconstructed mesh and mesh rendering image under two different time frame and camera view. The results shows our method achieves best mesh reconstruction as well as rendering quality. From Fig. 5 - Fig. 8 are the results on the D-NeRF dataset, our method also gives both mesh reconstruction and rendering quality in general.

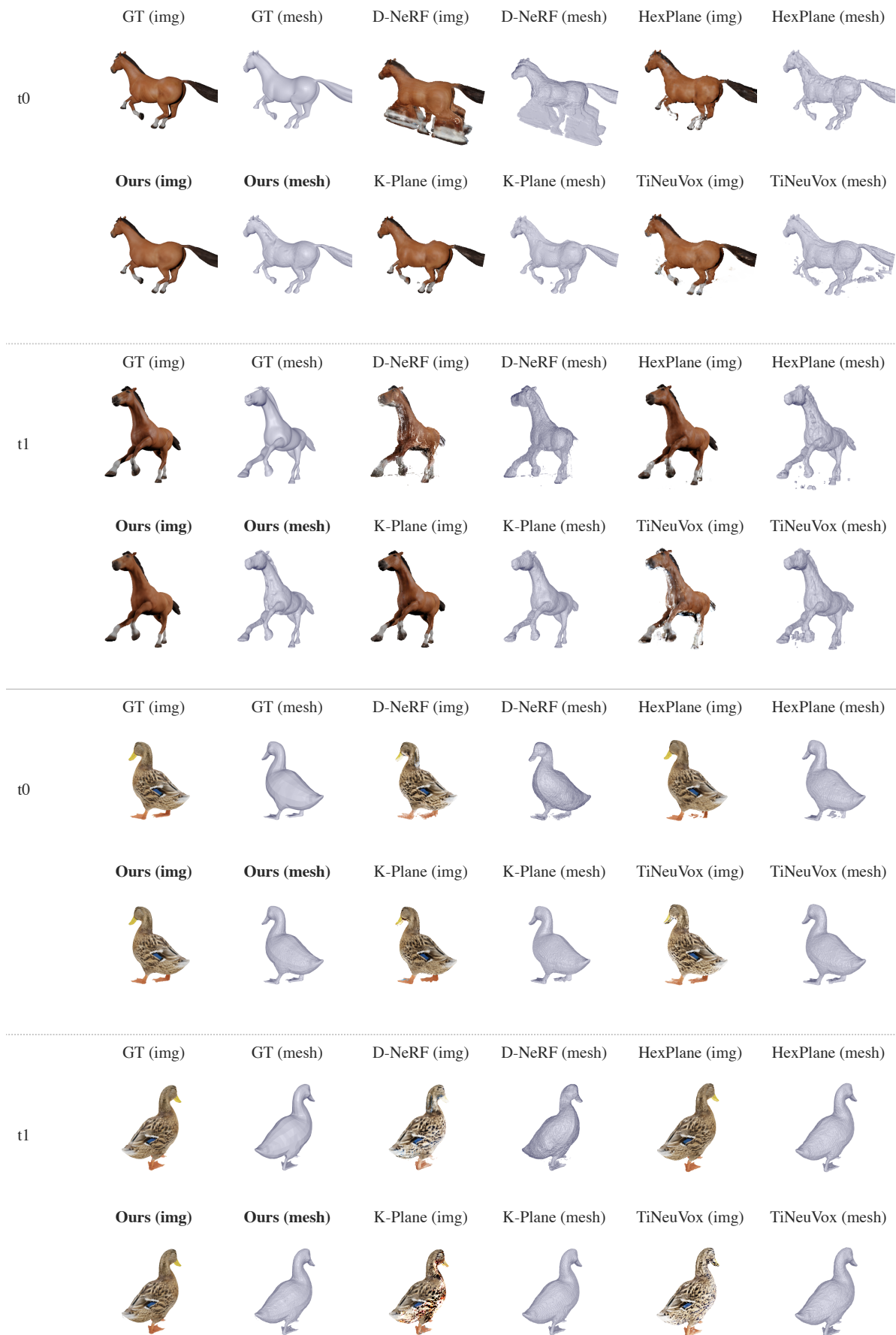


Fig. 2: Result comparison on the DG-Mesh dataset. We show the reconstructed mesh and the mesh rendering image. Our method reconstructs better geometry and appearance than other baselines.



Fig. 3: Result comparison on the DG-Mesh dataset. We show the reconstructed mesh and the mesh rendering image. Our method reconstructs better geometry and appearance than other baselines.

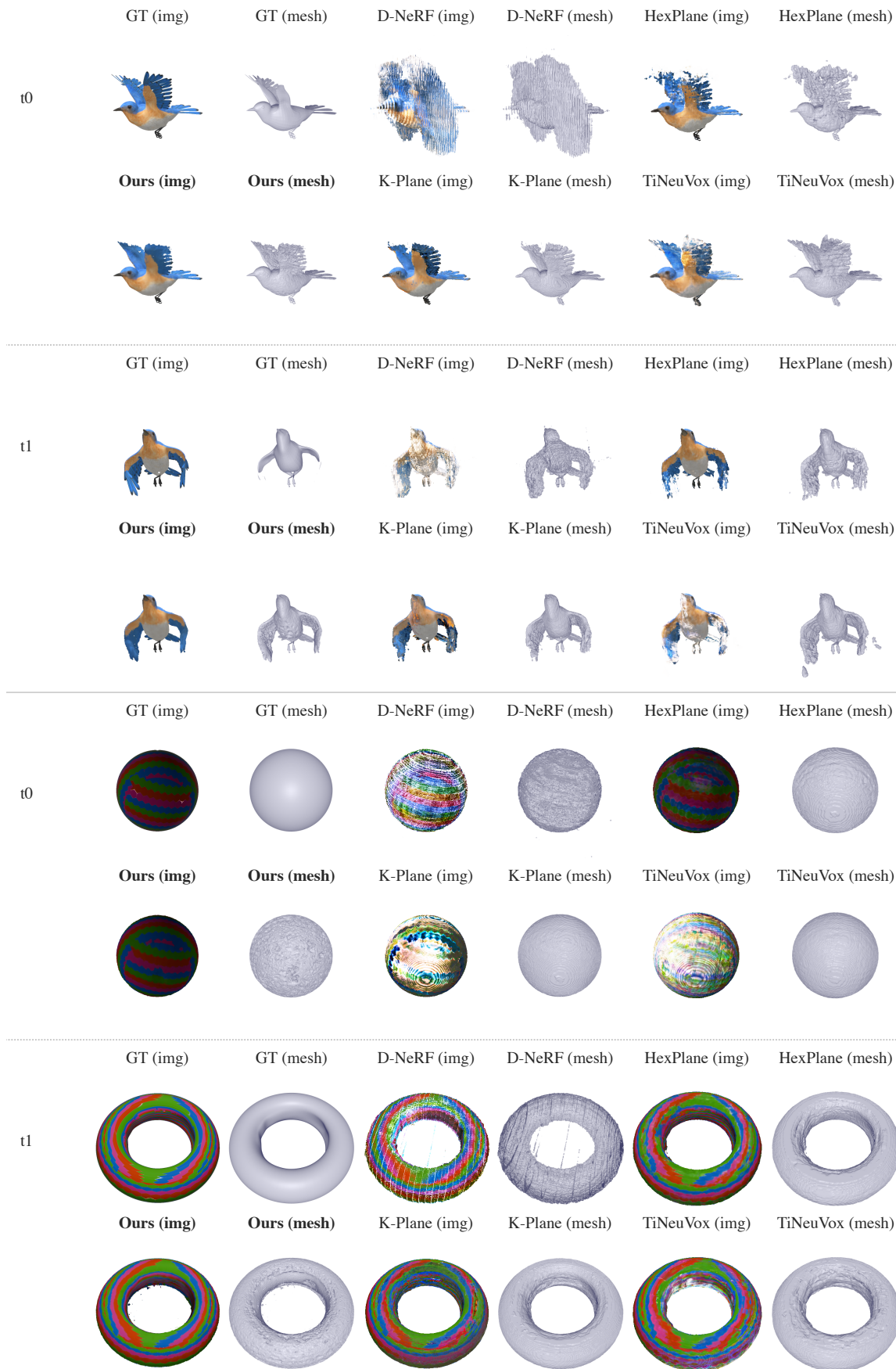


Fig. 4: Result comparison on the DG-Mesh dataset. We show the reconstructed mesh and the mesh rendering image. Our method reconstructs better geometry and appearance than other baselines.



Fig. 5: Result comparison on the D-NeRF dataset. We show the reconstructed mesh and the mesh rendering image. Our method reconstructs better geometry and appearance than other baselines.

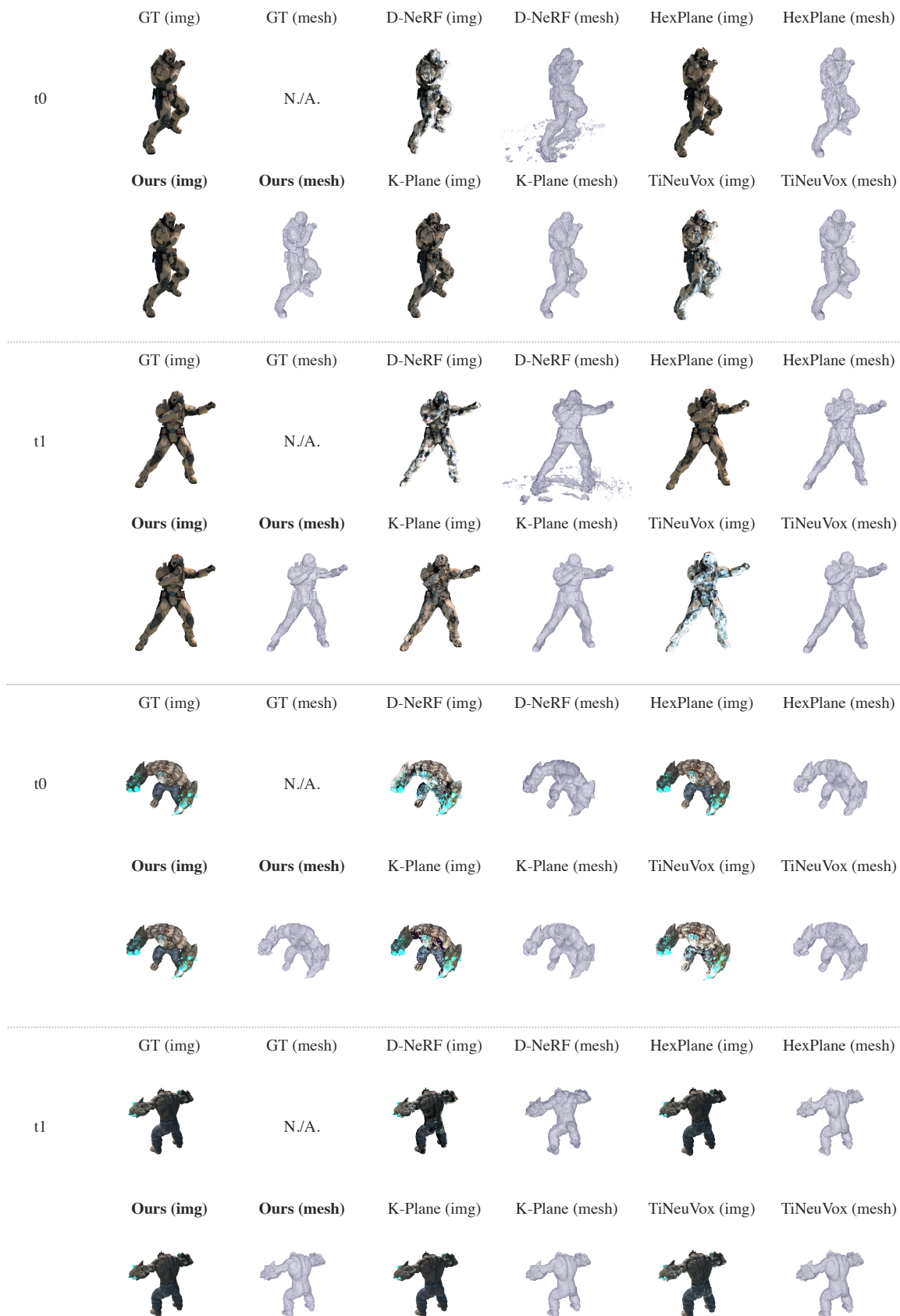


Fig. 6: Result comparison on the D-NeRF dataset. We show the reconstructed mesh and the mesh rendering image. Our method reconstructs better geometry and appearance than other baselines.

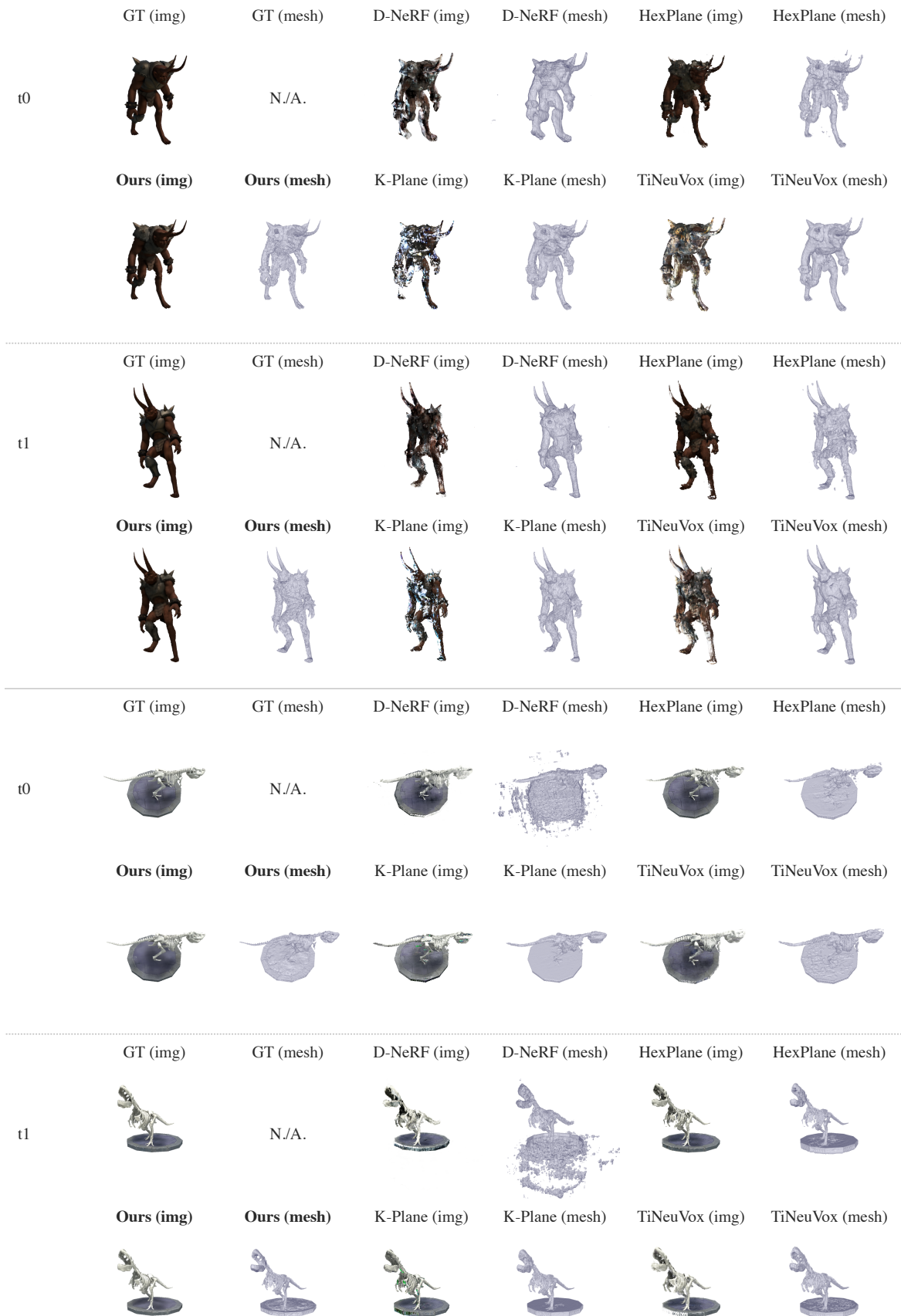


Fig. 7: Result comparison on the D-NeRF dataset. We show the reconstructed mesh and the mesh rendering image. Our method reconstructs better geometry and appearance than other baselines.

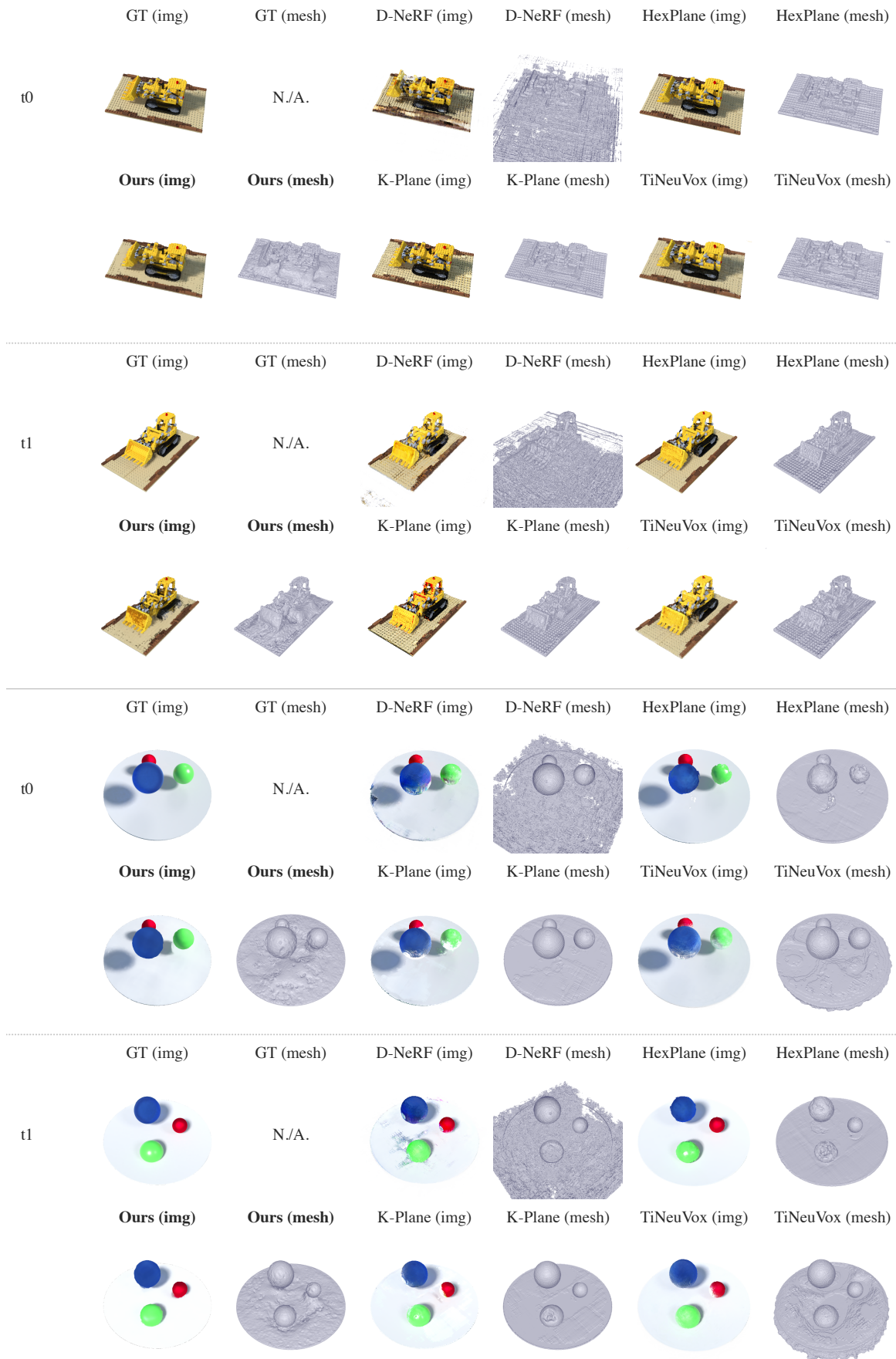


Fig. 8: Result comparison on the D-NeRF dataset. We show the reconstructed mesh and the mesh rendering image. Our method reconstructs better geometry and appearance than other baselines.